



THE UNIVERSITY *of* EDINBURGH

Edinburgh Research Explorer

Numerical algorithms for solving shallow water hydro-sediment-morphodynamic equations

Citation for published version:

Borthwick, A, Xia, C, Cao, Z & Pender, G 2017, 'Numerical algorithms for solving shallow water hydro-sediment-morphodynamic equations' *Engineering Computations*, vol. 34, no. 8, pp. 2836-2861. DOI: 10.1108/EC-01-2016-0026

Digital Object Identifier (DOI):

[10.1108/EC-01-2016-0026](https://doi.org/10.1108/EC-01-2016-0026)

Link:

[Link to publication record in Edinburgh Research Explorer](#)

Document Version:

Peer reviewed version

Published In:

Engineering Computations

General rights

Copyright for the publications made accessible via the Edinburgh Research Explorer is retained by the author(s) and / or other copyright owners and it is a condition of accessing these publications that users recognise and abide by the legal requirements associated with these rights.

Take down policy

The University of Edinburgh has made every reasonable effort to ensure that Edinburgh Research Explorer content complies with UK legislation. If you believe that the public display of this file breaches copyright please contact openaccess@ed.ac.uk providing details, and we will remove access to the work immediately and investigate your claim.



1 **Numerical Algorithms for Solving Shallow Water Hydro-Sediment-Morphodynamic**
2 **Equations**

3
4 **Chunchen Xia**

5 PhD student, *State Key Laboratory of Water Resources and Hydropower Engineering Science,*
6 *Wuhan University, Wuhan, China.*
7 *Email: xcc@whu.edu.cn*

8
9 **Zhixian Cao**

10 Professor, *State Key Laboratory of Water Resources and Hydropower Engineering Science,*
11 *Wuhan University, Wuhan, China; and Professor, Institute for Infrastructure and Environment,*
12 *Heriot-Watt University, Edinburgh, UK.*
13 *Email: zxcao@whu.edu.cn*

14
15 **Gareth Pender**

16 Professor, *Institute for Infrastructure and Environment, Heriot-Watt University, Edinburgh, UK;*
17 *and Guest Professor, State Key Laboratory of Water Resources and Hydropower Engineering*
18 *Science, Wuhan University, Wuhan, China.*
19 *Email: g.pender@hw.ac.uk*

20
21 **Alistair G.L. Borthwick**

22 Professor, *School of Engineering, University of Edinburgh, The King's Buildings, Edinburgh, UK;*
23 *and Guest Professor, State Key Laboratory of Water Resources and Hydropower Engineering*
24 *Science, Wuhan University, Wuhan, China.*
25 *Email: Alistair.Borthwick@ed.ac.uk*

30 **ABSTRACT**

31 **Purpose** - The purpose of this paper is to present a new numerical algorithm for solving the
32 coupled shallow water hydro-sediment-morphodynamic equations governing fluvial processes,
33 and also to clarify the performance of the conventional algorithm, which redistributes the variable
34 water-sediment mixture density to the source terms of the governing equations and accordingly
35 the hyperbolic operator is rendered similar to that of the conventional shallow water equations for
36 clear water flows.

37 **Design/methodology/approach** - The coupled shallow water hydro-sediment-morphodynamic
38 equations governing fluvial processes are arranged in full conservation form, and solved by a
39 well-balanced weighted surface depth gradient method along with a slope-limited centred scheme.
40 The present algorithm is verified for a spectrum of test cases, which involve complex flows with
41 shock waves and sediment transport processes with contact discontinuities over irregular
42 topographies. The conventional algorithm is evaluated as compared to the present algorithm and
43 available experimental data.

44 **Findings** - The new algorithm performs satisfactorily over the spectrum of test cases, and the
45 conventional algorithm is confirmed to work similarly well.

46 **Originality/value** – A new numerical algorithm, without redistributing the water-sediment
47 mixture density, is proposed for solving the coupled shallow water hydro-sediment-
48 morphodynamic equations. It is clarified that the conventional algorithm, involving redistribution
49 of the water-sediment mixture density, performs similarly well. Both algorithms appear equally
50 applicable to problems encountered in computational river modelling.

51 **Keywords** Shallow water hydro-sediment-morphodynamic equations, Well-balanced, Coupled,
52 Finite volume method, Fluvial processes

53 **Paper type** Research paper

54

55 **1. Introduction**

56 The interactive processes of flow, sediment transport and morphological evolution influenced by
57 both human activities and extreme natural events constitute a hierarchy of physical problems of
58 significant interest in the fields of fluvial hydraulics and geomorphology. Great efforts have been
59 made to establish refined numerical models and to test the models over a range of scales in
60 laboratory and field experiments (Bellos et al. 1992, Fraccarollo and Toro 1995, Capart and
61 Young 1998, Fraccarollo and Capart 2002, Leal et al. 2006, Spinewine and Zech 2007).

62 The last several decades have witnessed rapid development and widespread applications of the
63 complete shallow water hydro-sediment-morphodynamic (SHSM) equations, which explicitly
64 accommodate interactions between flow, sediment transport and bed evolution in a coupled
65 manner and adopt a non-capacity sediment transport approach based on physical perspectives
66 (Cao et al. 2004, Wu and Wang 2007). An increasing number of computational studies in
67 hydraulic engineering and geomorphological studies are based on the SHSM equations, for
68 example, dam-break floods over erodible bed (Cao et al. 2004, Wu and Wang 2007, Xia et al.
69 2010, Huang et al. 2012, Huang et al. 2014), coastal processes (Xiao et al. 2010, Kim 2015, Zhu
70 and Dodd 2015), watershed erosion processes (Kim et al. 2013), and turbidity currents (Hu et al.
71 2012, Cao et al. 2015). as well as rainfall-runoff processes (Li and Duffy 2011).

72 The finite volume method (FVM) is one of the most promising methods for solving the SHSM
73 equations. Pivotal to this method is the determination of the numerical flux in cases where the
74 dependent variables may be steep-fronted or have discontinuous gradients. A series of numerical
75 schemes are available in this regard, such as the Harten-Lax-van Leer (HLL) scheme (Harten et al.
76 1983, Simpson and Castelltort 2006, Wu et al. 2012), the Harten-Lax-van Leer contact wave
77 (HLLC) scheme (Toro et al. 1994, Cao et al. 2004, Zhang and Duan 2011, Yue et al. 2015), the
78 Roe scheme (Roe 1981, Leighton et al. 2010, Xia et al. 2010, Li and Duffy 2011), and the slope
79 limited centred (SLIC) scheme (Toro 1999, Hu and Cao 2009, Qian et al. 2015). In recent years,

80 well-balanced schemes have been developed to improve the handling of source terms in numerical
81 models and extend their applications to irregular topographies.

82 In practice, it is usual to manipulate the original SHSM equations into a form that eliminates the
83 variable water-sediment mixture density on the left-hand-side (LHS) of the governing equations
84 leading to the conventional numerical algorithm (CNA) which is an extension of existing
85 numerical schemes for shallow water equations of clear water flows (Cao et al. 2004, Simpson
86 and Castellort 2006, Wu and Wang 2008, Xia et al. 2010, Zhang and Duan 2011, Yue et al. 2015).
87 However, it has so far remained poorly understood whether the equation manipulation could incur
88 conservation errors due to the splitting of certain product derivatives by the chain rule and the
89 reassignment of the split forms to flux gradient and source terms. Given this observation, a fully
90 conservative numerical algorithm (FCNA) is proposed herewith to directly solve the original
91 SHSM equations in which the mixture density is maintained on the LHS. Numerical fluxes and
92 the bed slope source terms are estimated by the well-balanced, weighted surface depth gradient
93 method (WSDGM) version of the SLIC scheme. The remainder of the paper is organized as
94 follows. First, the governing equations are presented in the CNA and FCNA forms. Second, the
95 numerical scheme used to solve the equations is outlined. Third, the CNA and FCNA are
96 examined to show their capability of preserving quiescent flow, and then the FCNA is verified for
97 several test cases, which involve complex flows with shock waves and also sediment transport
98 processes with contact discontinuities over irregular topographies. Meanwhile, the CNA is also
99 evaluated as compared to the FCNA and available experimental data. Finally, conclusions are
100 drawn from the present work.

101

102

103 2. Mathematical Model

104 2.1 Governing equations

105 The governing equations of SHSM models can be derived by directly applying the Reynolds
106 Transport Theorem in fluid dynamics (Batchelor 1967, Xie 1990), or by integrating and averaging
107 the three-dimensional mass and momentum conservation equations (Wu 2007). For ease of
108 description, consider longitudinally one-dimensional flow over a mobile and mild-sloped bed
109 composed of uniform (single-sized) and non-cohesive sediment. The governing equations
110 comprise the mass and momentum conservation equations for the water-sediment mixture flow
111 and the mass conservation equations, respectively, for sediment and bed material. These constitute
112 a system of four equations and four physical variables (flow depth, depth-averaged velocity,
113 sediment concentration and bed elevation), which can be written as

$$114 \quad \frac{\partial(\rho h)}{\partial t} + \frac{\partial(\rho h u)}{\partial x} = -\rho_0 \frac{\partial z}{\partial t} \quad (1)$$

$$115 \quad \frac{\partial(\rho h u)}{\partial t} + \frac{\partial}{\partial x} \left(\rho h u^2 + \frac{1}{2} \rho g h^2 \right) = \rho g h \left(-\frac{\partial z}{\partial x} - S_f \right) \quad (2)$$

$$116 \quad \frac{\partial(hc)}{\partial t} + \frac{\partial(huc)}{\partial x} = E - D \quad (3)$$

$$117 \quad \frac{\partial z}{\partial t} = -\frac{E - D}{1 - p} \quad (4)$$

118 where t = time; x = streamwise coordinate; h = flow depth; u = depth-averaged flow velocity in x
119 direction; z = bed elevation; c = flux-averaged volumetric sediment concentration; g =
120 gravitational acceleration; $S_f = n^2 u^2 / h^{4/3}$ = friction slope, and n = Manning roughness; p = bed
121 sediment porosity; E, D = sediment entrainment and deposition fluxes across the bottom
122 boundary of flow, representing the sediment exchange between the water column and bed;
123 $\rho = \rho_w(1 - c) + \rho_s c$ = density of water-sediment mixture; $\rho_0 = \rho_w p + \rho_s(1 - p)$ = density of

124 saturated bed; and ρ_w, ρ_s = densities of water and sediment. Shape factors arising from depth-
 125 averaging manipulation in the preceding equations have been presumed to be equal to unity. The
 126 empirical relations for sediment exchange between the flow and the erodible bed will be
 127 introduced according to the specific test cases in Section 3. In order to facilitate mathematical
 128 manipulation and based on the fact that the bed deformation is solely determined by the local
 129 entrainment and deposition fluxes, Eq. (4) is isolated from Eqs. (1-3) and solved separately.

130

131 *2.2 Equations in traditional conservative form*

132 In the CNA, Eqs. (1) and (2) are reformulated by eliminating the water-sediment mixture density
 133 on the LHS using the relation $\rho = \rho_w(1-c) + \rho_s c$ and Eqs. (3) and (4). Accordingly, the
 134 hyperbolic operator is rendered similar to that of the conventional shallow water equations for
 135 clear water flows, as can be seen in Eqs. (5) and (6). This treatment was first proposed and
 136 implemented by Cao et al. (2004) and has been widely used in computational river modelling
 137 (Simpson and Castellort 2006, Wu and Wang 2007, Yue et al. 2008, Hu and Cao 2009, Xia et al.
 138 2010, Huang et al. 2014, Li et al. 2014, Cao et al. 2015). More broadly, the idea behind this
 139 numerical strategy has also been applied to solve shallow water equations including an effective
 140 porosity parameter to represent the effect of small-scale impervious obstructions on reducing the
 141 available storage volume and effective cross section of shallow water flows (Cea and Vázquez-
 142 Cendón 2010).

$$143 \quad \frac{\partial \mathbf{U}}{\partial t} + \frac{\partial \mathbf{F}}{\partial x} = \mathbf{S}_b + \mathbf{S}_f \quad (5)$$

144 where \mathbf{S}_b = vector of bed slope source term components; \mathbf{S}_f = vector of other source terms; \mathbf{U} and
 145 \mathbf{F} = vectors as follows,

146

$$\mathbf{U} = \begin{bmatrix} h \\ hu \\ hc \end{bmatrix} \quad \mathbf{F} = \begin{bmatrix} hu \\ hu^2 + \frac{1}{2}gh^2 \\ huc \end{bmatrix} \quad (6a, b)$$

147

$$\mathbf{S}_b = \begin{bmatrix} 0 \\ -gh \frac{\partial z}{\partial x} \\ 0 \end{bmatrix} \quad \mathbf{S}_f = \begin{bmatrix} (E-D)/(1-p) \\ -ghS_f - \frac{(\rho_s - \rho_w)gh^2}{2\rho} \frac{\partial c}{\partial x} - \frac{(\rho_0 - \rho)(E-D)u}{\rho(1-p)} \\ E-D \end{bmatrix} \quad (6c, d)$$

148

149 *2.3 Equations in new conservative form*

150 In the FCNA, Eqs. (1)-(4) are solved directly, without first redistributing the water-sediment
 151 mixture density as in the CNA. If ρh and c/ρ are regarded as independent variables
 152 respectively, Eqs. (1)-(3) can be written in the conservative form of Eq. (5), with vectors
 153 expressed in terms of variables $[\rho h \quad u \quad c/\rho]^T$, as follows,

154

$$\mathbf{U} = \begin{bmatrix} \rho h \\ \rho hu \\ \rho h \frac{c}{\rho} \end{bmatrix} \quad \mathbf{F} = \begin{bmatrix} \rho hu \\ \rho hu^2 + \frac{g}{2\rho}(\rho h)^2 \\ \rho hu \frac{c}{\rho} \end{bmatrix} \quad (7a,b)$$

155

$$\mathbf{S}_b = \begin{bmatrix} 0 \\ -\rho gh \frac{\partial z}{\partial x} \\ 0 \end{bmatrix} \quad \mathbf{S}_f = \begin{bmatrix} \rho_0(E-D)/(1-p) \\ -\rho ghS_f \\ E-D \end{bmatrix} \quad (7c,d)$$

156

157 *2.4 Numerical scheme*

158 *2.4.1 Finite volume discretization*

159 Implementing the finite volume discretization along with the operator-splitting method for Eq. (5),
 160 one obtains (Aureli et al. 2008, Hu et al. 2012, Hu et al. 2015, Qian et al. 2015)

161
$$\mathbf{U}_i^* = \mathbf{U}_i^n - \frac{\Delta t}{\Delta x} (\mathbf{F}_{i+1/2}^n - \mathbf{F}_{i-1/2}^n) + \Delta t \mathbf{S}_{bi} \quad (8a)$$

162
$$\mathbf{U}_i^{n+1} = \mathbf{U}_i^* + \Delta t \mathbf{S}_f^{RK} \quad (8b)$$

163 where Δt = time step; Δx = spatial step; i = spatial node index; n = time node index; $\mathbf{F}_{i+1/2}$ = inter-
 164 cell numerical flux at $x = x_{i+1/2}$; and the source term \mathbf{S}_f^{RK} is solved by the third-order Runge-Kutta
 165 (RK) method (Gottlieb and Shu 1998)

166
$$\mathbf{S}_f^{RK} = \frac{1}{6} [\mathbf{S}_f(\mathbf{U}_i^{*1}) + 4\mathbf{S}_f(\mathbf{U}_i^{*2}) + \mathbf{S}_f(\mathbf{U}_i^{*3})] \quad (9)$$

167
$$\mathbf{U}_i^{*1} = \mathbf{U}_i^* \quad (10a)$$

168
$$\mathbf{U}_i^{*2} = \mathbf{U}_i^{*1} + \frac{\Delta t}{2} \mathbf{S}_f(\mathbf{U}_i^{*1}) \quad (10b)$$

169
$$\mathbf{U}_i^{*3} = 2[\mathbf{U}_i^{*1} + \Delta t \mathbf{S}_f(\mathbf{U}_i^{*2})] - [\mathbf{U}_i^{*1} + \Delta t \mathbf{S}_f(\mathbf{U}_i^{*1})] \quad (10c)$$

170 The bed deformation is updated by the discretization of Eq. (4)

171
$$z_i^{n+1} = z_i^n + \Delta t \frac{(D-E)_i^{RK}}{(1-p)} \quad (11)$$

172 For numerical stability, the time step satisfies the Courant–Friedrichs–Lewy (CFL) condition

173
$$\Delta t = \frac{C_r}{\lambda_{\max} / \Delta x} \quad (12)$$

174 where C_r is the Courant number and $C_r < 1$; and λ_{\max} is the maximum celerity computed from the
 175 Jacobian matrix $\partial \mathbf{F} / \partial \mathbf{U}$.

176 2.4.2 Well-balanced version of the SLIC scheme

177 Unlike certain well-balanced numerical schemes which directly adopt the water surface elevation
 178 as a flow variable in their rearranged SHSM equations (Rogers et al. 2003, Liang and Borthwick

179 2009, Liang and Marche 2009, Huang et al. 2012, Huang et al. 2014, Qian et al. 2015), the present
 180 model maintains the original equations, with the water depth variable evaluated from a weighted
 181 average of the slope limited water depth and water surface elevation (Zhou et al. 2001, Aureli et
 182 al. 2008, Hu et al. 2012) in the framework of the SLIC scheme that results from replacing the
 183 Godunov flux by the FORCE flux in the MUSCL-Hancock scheme (Toro 2001). The original
 184 SLIC scheme (Toro 2001, Aureli et al. 2004) is termed a depth-gradient method (DGM) version
 185 because it uses the spatial gradient of the water depth for the interpolation, and is robust and stable
 186 for cases involving high gradient in water level provided the bathymetry has small gradient. The
 187 scheme is also capable of tracking the motion of wetting and drying fronts above a threshold flow
 188 depth h_{lim} as discussed in Section 2.4.3. However, when the bed topography is irregular and has
 189 large spatial gradient, the DGM version may not reproduce the exact solution for stationary flows
 190 (i.e., it does not satisfy the exact *C-property* (Bermudez and Vazquez 1994)) because of the
 191 imbalance between the bed slope source term and flux gradient. The *C-property* can be instead
 192 satisfied by the surface gradient method (SGM) proposed by Zhou et al. (2001), which is
 193 preferable for cases when small gradient in water level occurs alongside high gradient in water
 194 depth. However this method still has certain limitations in the treatment of the wetting and drying
 195 fronts that may lead to unphysical results (Aureli et al. 2008). To exploit the advantages of both
 196 DGM and SGM, the well-balanced WSDGM version of the SLIC scheme has been put forward
 197 by Aureli et al. (2008), and is employed herein to estimate the numerical fluxes as well as the bed
 198 slope source term in Eq. (8a). This method involves following three steps (Aureli et al. 2008, Hu
 199 et al. 2015). Figure 1 provides a definition sketch.

200 ***Step 1:*** Data reconstruction

201 For ease of description, a new vector of dependent variables \mathbf{Q} is introduced, with

202 $\mathbf{Q}_{TNA} = [h \quad hu \quad hc \quad h+z \quad z]^T$ and $\mathbf{Q}_{NNA} = \left[\rho h \quad \rho hu \quad \rho h \frac{c}{\rho} \quad \rho h + \rho z \quad \rho z \right]^T$ indicating the

203 conventional and fully conservative algorithms respectively. The first four boundary extrapolated

204 variables $\mathbf{Q}_{i+1/2}^L$ and $\mathbf{Q}_{i+1/2}^R$ are evaluated at the left and right sides of interface $x = x_{i+1/2}$ to achieve
 205 second-order accuracy in space.

$$206 \quad \mathbf{Q}_{i+1/2}^L = \mathbf{Q}_i^n + \phi_{i-1/2}^L \frac{\mathbf{Q}_i^n - \mathbf{Q}_{i-1}^n}{2} \quad (13a)$$

$$207 \quad \mathbf{Q}_{i+1/2}^R = \mathbf{Q}_{i+1}^n - \phi_{i+3/2}^R \frac{\mathbf{Q}_{i+2}^n - \mathbf{Q}_{i+1}^n}{2} \quad (13b)$$

208 where ϕ = slope limiter, which is a function of the ratios $r^{L,R}$ of variables \mathbf{Q} . Here the Minmod
 209 limiter is used, which reads

$$210 \quad \phi(r) = \begin{cases} \min(r, 1) & \text{if } r > 0 \\ 0 & \text{if } r \leq 0 \end{cases} \quad (14)$$

211 with

$$212 \quad r_{i-1/2}^L = \frac{\mathcal{Q}_{i+1}^n - \mathcal{Q}_i^n}{\mathcal{Q}_i^n - \mathcal{Q}_{i-1}^n} \quad r_{i+3/2}^R = \frac{\mathcal{Q}_{i+1}^n - \mathcal{Q}_i^n}{\mathcal{Q}_{i+2}^n - \mathcal{Q}_{i+1}^n} \quad (15a, b)$$

213 The last elements of $\mathbf{Q}_{i+1/2}^L$ and $\mathbf{Q}_{i+1/2}^R$ are evaluated at the interface $x = x_{i+1/2}$, such that,

$$214 \quad \mathbf{Q}_{i+1/2}^L(5) = \mathbf{Q}_{i+1/2}^R(5) = \frac{1}{2}(\mathbf{Q}_i^n(5) + \mathbf{Q}_{i+1}^n(5)) \quad (16)$$

215 The first elements of $\mathbf{Q}_{i+1/2}^L$ and $\mathbf{Q}_{i+1/2}^R$ are updated by a weighted average of boundary
 216 extrapolated values derived from MUSCL DGM and SGM extrapolations as follows:

$$217 \quad \mathbf{Q}_{i+1/2}^L(1) = \phi \mathbf{Q}_{i+1/2}^L(1) + (1 - \phi) [\mathbf{Q}_{i+1/2}^L(4) - \mathbf{Q}_{i+1/2}^L(5)] \quad (17a)$$

$$218 \quad \mathbf{Q}_{i+1/2}^R(1) = \phi \mathbf{Q}_{i+1/2}^R(1) + (1 - \phi) [\mathbf{Q}_{i+1/2}^R(4) - \mathbf{Q}_{i+1/2}^R(5)] \quad (17b)$$

219 where ϕ = weighting factor between the DGM and SGM with $0 \leq \phi \leq 1$, which is specified as a
 220 function of the Froude number,

$$\phi = \begin{cases} 0.5 \left[1 - \cos \left(\frac{\pi Fr}{Fr_{\text{lim}}} \right) \right] & 0 \leq Fr \leq Fr_{\text{lim}} \\ 1 & Fr > Fr_{\text{lim}} \end{cases} \quad (18)$$

where Fr_{lim} is an upper limit beyond which a pure DGM reconstruction is performed. In this paper, $Fr_{\text{lim}} = 2.0$ is adopted according to Aureli et al. (2008).

Boundary extrapolated vectors $\mathbf{Q}_{i+1/2}^L$ and $\mathbf{Q}_{i+1/2}^R$ are used to update the vectors of conserved variables of the governing equations as follows

$$\mathbf{U}_{i+1/2}^L = \left[\mathbf{Q}_{i+1/2}^L(1) \quad \mathbf{Q}_{i+1/2}^L(2) \quad \mathbf{Q}_{i+1/2}^L(3) \right]^T \quad (19a)$$

$$\mathbf{U}_{i+1/2}^R = \left[\mathbf{Q}_{i+1/2}^R(1) \quad \mathbf{Q}_{i+1/2}^R(2) \quad \mathbf{Q}_{i+1/2}^R(3) \right]^T \quad (19b)$$

Step 2: Evolution of extrapolated variables

The boundary extrapolated conserved variables are further evolved over $\Delta t / 2$ to achieve second-order accuracy in time. In order to satisfy the *C-property* when WSDGM is adopted, the contribution due to gravity must be included

$$\bar{\mathbf{U}}_{i+1/2}^L = \mathbf{U}_{i+1/2}^L - \frac{\Delta t / 2}{\Delta x} \left[\mathbf{F}(\mathbf{U}_{i+1/2}^L) - \mathbf{F}(\mathbf{U}_{i-1/2}^R) \right] + \frac{\Delta t}{2} \mathbf{S}_{bi} \quad (20a)$$

$$\bar{\mathbf{U}}_{i+1/2}^R = \mathbf{U}_{i+1/2}^R - \frac{\Delta t / 2}{\Delta x} \left[\mathbf{F}(\mathbf{U}_{i+3/2}^L) - \mathbf{F}(\mathbf{U}_{i+1/2}^R) \right] + \frac{\Delta t}{2} \mathbf{S}_{bi+1} \quad (20b)$$

where \mathbf{S}_{bi} in Eqs. (20a) and (20b) are discretized using central-differences with extrapolated variables taken from Step 1 and $z_{i+1/2} = (z_{i+1} + z_i) / 2$.

$$\mathbf{S}_{bi} = \begin{bmatrix} 0 \\ -g \left[\mathbf{U}_{i+1/2}^L(1) + \mathbf{U}_{i-1/2}^R(1) \right] (z_{i+1/2} - z_{i-1/2}) / (2\Delta x) \\ 0 \end{bmatrix} \quad (21)$$

Step 3: Numerical fluxes and bed slope source term

238 The numerical fluxes are estimated by the FORCE (first-order centred) approximate Riemann
 239 solver, which is an average of the Lax–Friedrichs flux \mathbf{F}^{LF} and the two-step Lax–Wendroff flux
 240 \mathbf{F}^{LW2} (Toro 2001)

$$241 \quad \mathbf{F}_{i+1/2} = (\mathbf{F}_{i+1/2}^{LW2} + \mathbf{F}_{i+1/2}^{LF}) / 2 \quad (22)$$

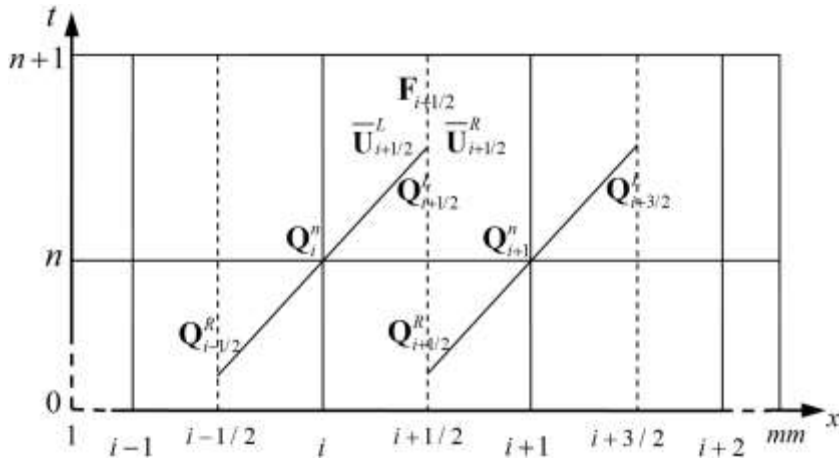
$$242 \quad \mathbf{F}_{i+1/2}^{LW2} = \mathbf{F}(\mathbf{U}_{i+1/2}^{LW2}) \quad (23a)$$

$$243 \quad \mathbf{U}_{i+1/2}^{LW2} = \frac{1}{2}(\bar{\mathbf{U}}_{i+1/2}^R + \bar{\mathbf{U}}_{i+1/2}^L) - \frac{1}{2} \frac{\Delta t}{\Delta x} (\mathbf{F}(\bar{\mathbf{U}}_{i+1/2}^R) - \mathbf{F}(\bar{\mathbf{U}}_{i+1/2}^L)) \quad (23b)$$

$$244 \quad \mathbf{F}_{i+1/2}^{LF} = \frac{1}{2}(\mathbf{F}(\bar{\mathbf{U}}_{i+1/2}^R) + \mathbf{F}(\bar{\mathbf{U}}_{i+1/2}^L)) - \frac{1}{2} \frac{\Delta x}{\Delta t} (\bar{\mathbf{U}}_{i+1/2}^R - \bar{\mathbf{U}}_{i+1/2}^L) \quad (24)$$

245 Finally, the bed slope source term in Eq. (8a) is computed using the evolved variables from Step 2,

$$246 \quad \mathbf{S}_{bi} = \begin{bmatrix} 0 \\ -g [\bar{\mathbf{U}}_{i+1/2}^L(1) + \bar{\mathbf{U}}_{i-1/2}^R(1)] (z_{i+1/2} - z_{i-1/2}) / (2\Delta x) \\ 0 \end{bmatrix} \quad (25)$$



247
 248 **Figure 1.** Sketch of the WSDGM version of the SLIC scheme

249
 250 **2.4.3 Wet/dry front**

251 In order to satisfy the *C-property*, a special treatment is performed at a wet-dry front. A threshold
 252 flow depth h_{lim} is used to judge whether the cell is dry or wet. Two neighboring cells will be

253 defined as the wet/dry front if one is wet and the other is dry. If the water surface of the wet cell is
254 lower than the bed elevation of its adjacent dry cell, the bed elevation and water surface of the dry
255 cell are set to be the water level of the wet cell and, consequently, the water depth is zero when
256 computing the numerical flux. The threshold flow depth h_{lim} is a model parameter and should be
257 sufficiently small for quantitative accuracy. A value of $h_{\text{lim}} = 1 \times 10^{-6}$ is adopted in the present
258 work.

259

260

261 3. Test Cases

262 A series of test cases is presented to verify the performance of the FCNA, accompanied by
263 comparisons with the CNA using the same numerical scheme. The test cases include steady flow
264 at equilibrium conditions over a steep bump (Aureli et al. 2008) (Case 1) to examine satisfaction
265 of the *C-property*, a density dam break with a single and two initial discontinuities without bed
266 deformation (Leighton et al. 2010) (Cases 2 and 3), dam-break over erodible beds at prototype-
267 scale (Cao et al. 2004) (Case 4) and laboratory-scale (Fraccarollo and Capart 2002) (Case 5), and
268 a reproduction of a large-scale flume experiment of landslide dam failure (Cao et al. 2011a)
269 (Case 6). The spatial step Δx is set specifically for different cases and the time step Δt then
270 obtained according to the CFL stability requirement of Eq. (12), as listed in Table I. In Case 5,
271 the flow depth temporal and spatial scales are so small that a relatively large frictional source term
272 may lead to numerical instability even if the CFL condition is satisfied. Thus a sub-time step Δt_σ
273 is deployed when updating the solutions to the next time step in Eq. (8b) of Case 5, following
274 Qian et al. (2015). It should be noted that the maximum sub-time step Δt_s in Qian et al. (2015)
275 was derived for the second-order R-K method. For the third-order R-K method (Gear 1971) used
276 herein, the maximum sub-time step is similarly derived, giving $\Delta t_s = 2.51h^{4/3} / gn^2u$. Table II
277 summarizes the parameter values for the different test cases.

278

279 **Table I.** Spatial increment and Courant number used in test cases

Test case	1	2	3	4	5	6
Spatial step Δx (m)	0.05	0.02	0.02	10	0.005	0.04
Courant number C_r	0.95	0.95	0.95	0.95	0.95	0.95

280

281 **Table II.** Summary of test cases

Test case	Sediment density ρ_s (kg/m ³)	Water density ρ_w (kg/m ³)	Gravitational acceleration g (m/s ²)	Sediment diameter d (mm)	Manning roughness n	Sediment porosity p
1	2,650	1,000	9.8	N/A	0.0	N/A
2	10.0	1.0	1.0	N/A	0.0	N/A
3	0.5&2.0	1.0	1.0	N/A	0.0	N/A
4	2,650	1,000	9.8	8.0	0.03	0.4
5*	1,540	1,000	9.8	3.5	0.025	0.3
6*	2,650	1,000	9.8	0.8	0.012	0.4

282 Notes: * Cases using measured data.

283 To quantify the differences between FCNA and CNA, as well as the discrepancies between the
 284 simulations and available experiment data, the non-dimensional discrepancy is defined based on
 285 the L^1 norm.

$$286 \quad L_{hz} = \frac{\sum abs[(h+z)_{TNA_i} - (h+z)_{NNA_i}]}{\sum abs[(h+z)_{TNA_i}]} \times 100\% \quad (26a)$$

$$287 \quad L_z = \frac{\sum abs(z_{TNA_i} - z_{NNA_i})}{\sum abs(z_{TNA_i})} \times 100\% \quad (26b)$$

$$288 \quad L_u = \frac{\sum abs(u_{TNA_i} - u_{NNA_i})}{\sum abs(u_{TNA_i})} \times 100\% \quad (26c)$$

289
$$L_c = \frac{\sum abs(c_{TNA_i} - c_{NNA_i})}{\sum abs(c_{TNA_i})} \times 100\% \quad (26d)$$

290
$$L_{hz}^* = \frac{\sum abs[(h+z)_i - (h+z)_{*i}]}{\sum abs[(h+z)_{*i}]} \times 100\% \quad (27)$$

291 where L_{hz} , L_z , L_u and L_c are the L^1 norms for stage, bed elevation, velocity and concentration
 292 used to compare FCNA with CNA. L_{hz}^* is the L^1 norm for stage used to compare the predictions
 293 by FCNA and CNA with measured data for Cases 5 and 6. Also, $h+z$, z , u and c are the
 294 predicted stage, bed elevation, velocity and concentration with subscripts FCNA and CNA
 295 denoting corresponding algorithms whilst $(h+z)_*$ and z_* are measured stage and bed elevation.

296

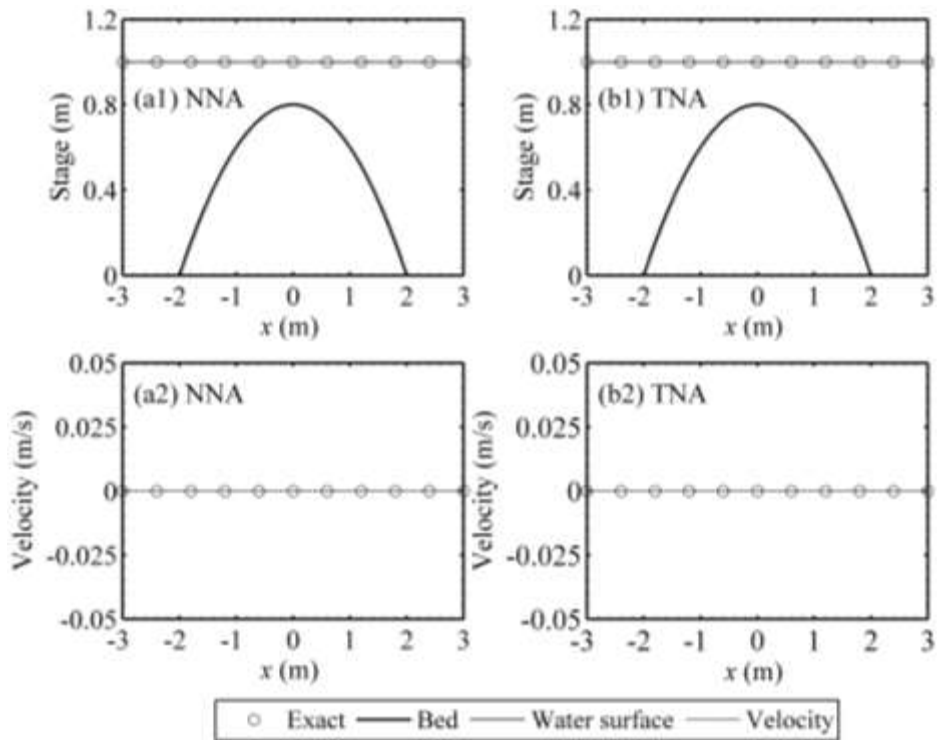
297 *3.1 Cases 1a and 1b: Steady flow at rest over a steep bump*

298 To test whether or not the numerical algorithms satisfy the *C-property* over irregular topography,
 299 a $[-10 \text{ m} \leq x \leq 10 \text{ m}]$ frictionless channel is considered with its bed profile characterized by the
 300 presence of a steep bump, described as (Liska and Wendroff 1998)

301
$$z(x) = \begin{cases} 0.8(1 - x^2/4) & -2 \text{ m} \leq x \leq 2 \text{ m} \\ 0 & \text{elsewhere} \end{cases} \quad (28)$$

302 Initially the flow is static and there is no water or sediment input at the inlet boundary. Two
 303 conditions of initial stage are considered. One is at the stage of 1.0 m (i.e., wet bed application),
 304 and the other is at the stage of 0.5 m (i.e., with wet-dry interfaces).

305 Figures 2 and 3 show the predicted stage and depth-averaged velocity profiles over the subdomain
 306 $[-3 \text{ m} \leq x \leq 3 \text{ m}]$ at time $t=1 \text{ h}$ obtained for the two initial stage conditions, using the FCNA and
 307 CNA. The initial steady, static equilibrium state is maintained by both algorithms, demonstrating
 308 that they are exactly well-balanced for cases with irregular topography irrespective of whether or
 309 not wet-dry interfaces are involved.

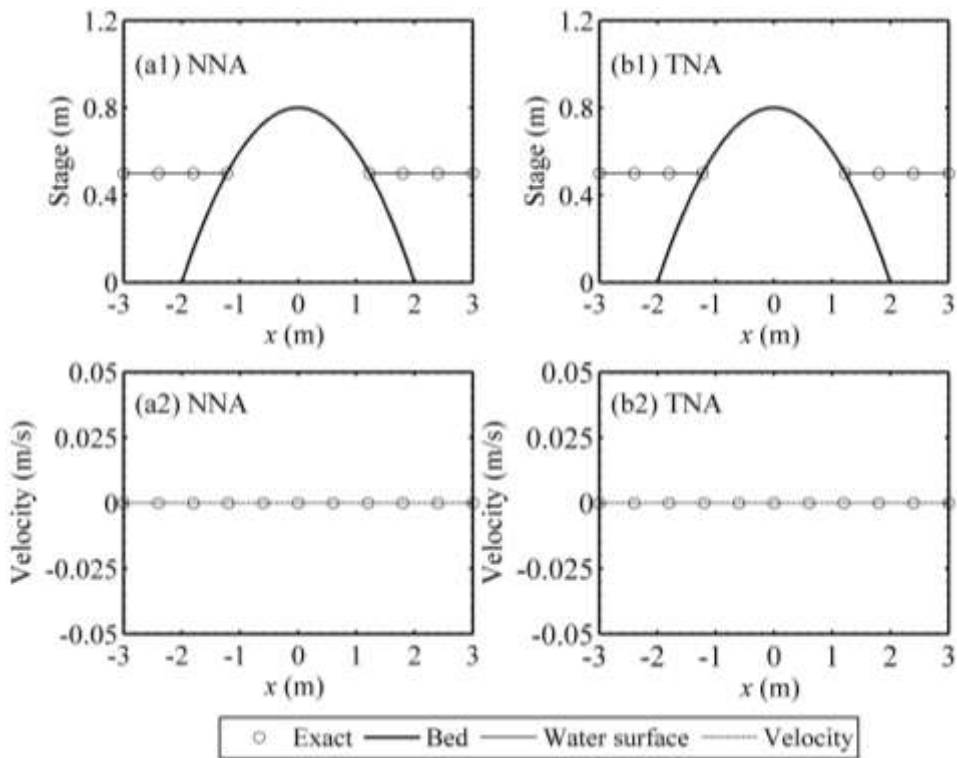


310

311 **Figure 2.** Case 1a: equilibrium stage and velocity profiles predicted by FCNA and CNA for initial

312

stage of 1.0 m



313

314 **Figure 3.** Case 1b: equilibrium stage and velocity profiles predicted by FCNA and CNA for

315

initial stage of 0.5 m

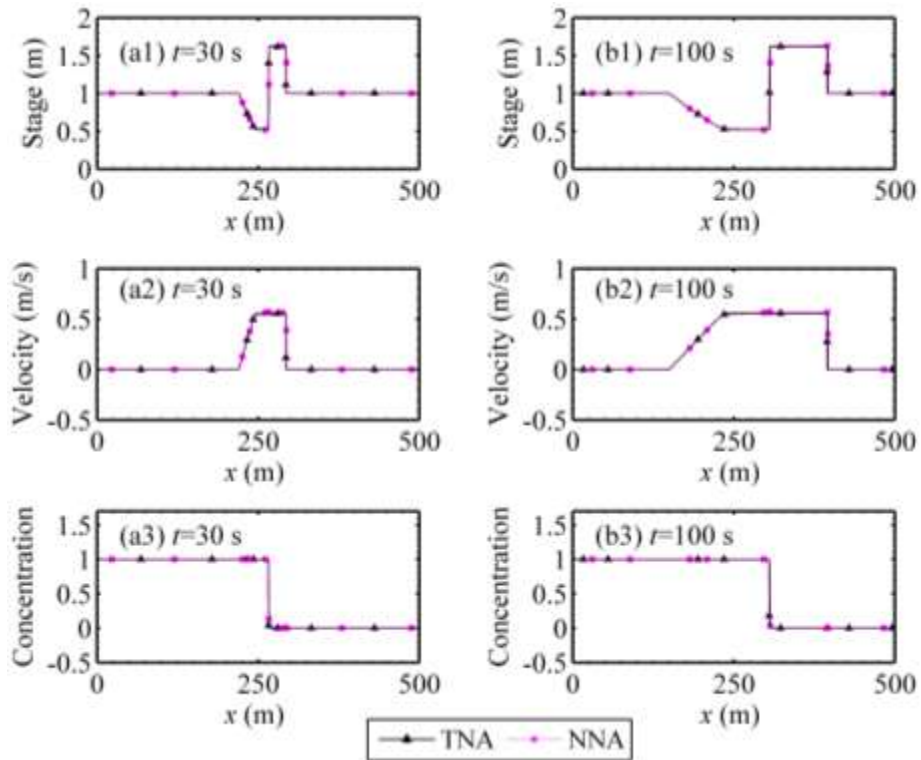
316

317 *3.2 Case 2: Density dam break with a single discontinuity*

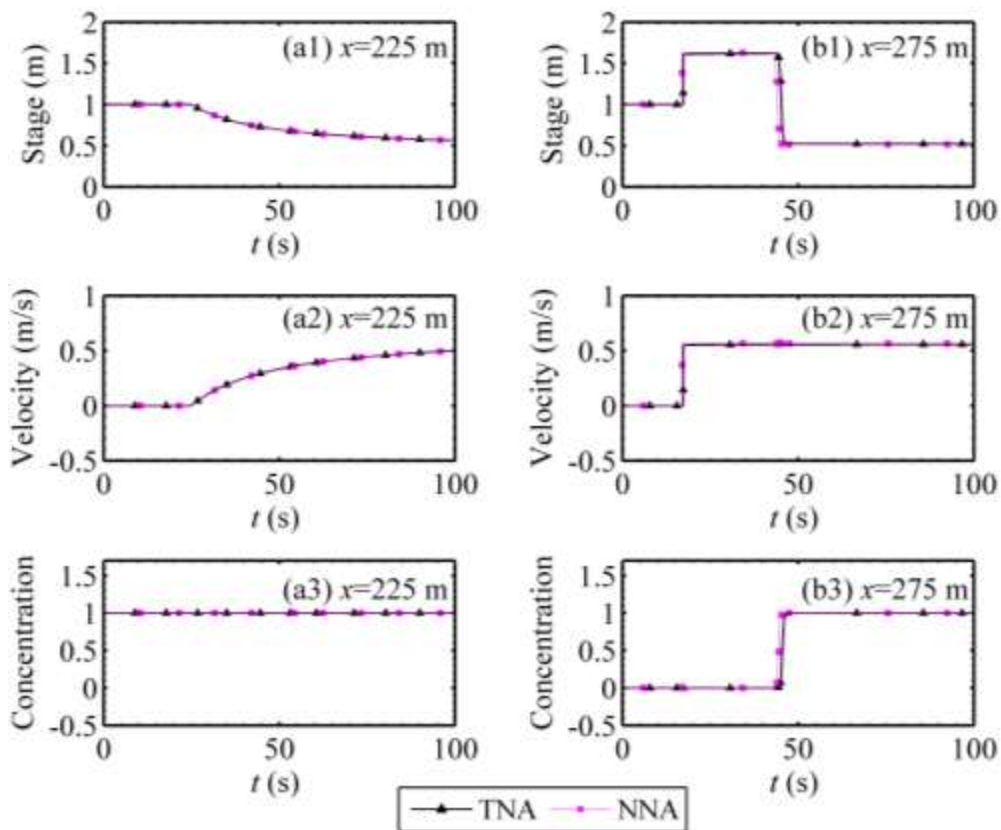
318 Attention is now focused on the initial and intermediate period following a dam break caused by
319 two adjacent liquids of different densities but equal initial stage. The horizontal and fixed channel
320 length is set to be $L = 500$ m, and the dam is located at the middle of the channel ($x = 250$ m).
321 Initially, the liquids in the channel are at rest with the same stage of 1 m, and the densities to the
322 left and right of the dam are $\rho_L = 10$ kg/m³ (concentration $c_L = 1$) and $\rho_R = 1$ kg/m³
323 (concentration $c_R = 0$), respectively.

324 Figure 4 shows the similarity between the stage, velocity and concentration profiles computed by
325 the FCNA and CNA at times $t = 30$ and 100 s. Figure 5 compares the predicted stage, velocity
326 and concentration time histories at sections $x = 225$ and 275 m (i.e. 25 m upstream and
327 downstream of the dam respectively), which indicate that the differences in results between the
328 two algorithms are trivial. Quantitatively, the values of L_{hz} , L_u and L_c are provided to highlight
329 the detailed differences between the FCNA and CNA, as given in Table III. It can be seen that the
330 values are almost the same at $x = 225$ m and increase a little but remain within 3% at $x = 275$ m.
331 Meanwhile, the values of L_{hz} , L_u and L_c at selected instants are within 1%, 3% and 0.5%
332 respectively, which demonstrate close agreement between the simulations produced by the two
333 algorithms.

334



335
 336 **Figure 4.** Case 2: stage and velocity profiles predicted by FCNA and CNA for density dam break
 337 with a single discontinuity at times: (a) $t = 30$ s; and (b) $t = 100$ s.



338
 339 **Figure 5.** Case 2: stage and velocity time histories predicted by FCNA and CNA for density dam
 340 break with a single discontinuity at locations: (a) $x = 225$ m; and (b) $x = 275$ m.

341

342 **Table III.** L_{hz} , L_u and L_c for Case 2

Location or Time	$x = 225$ m	$x = 275$ m	$t = 30$ s	$t = 100$ s
L_{hz} (%)	0.01	2.24	0.30	0.68
L_u (%)	0.02	2.07	2.92	1.95
L_c (%)	0.00	1.93	0.17	0.33

343

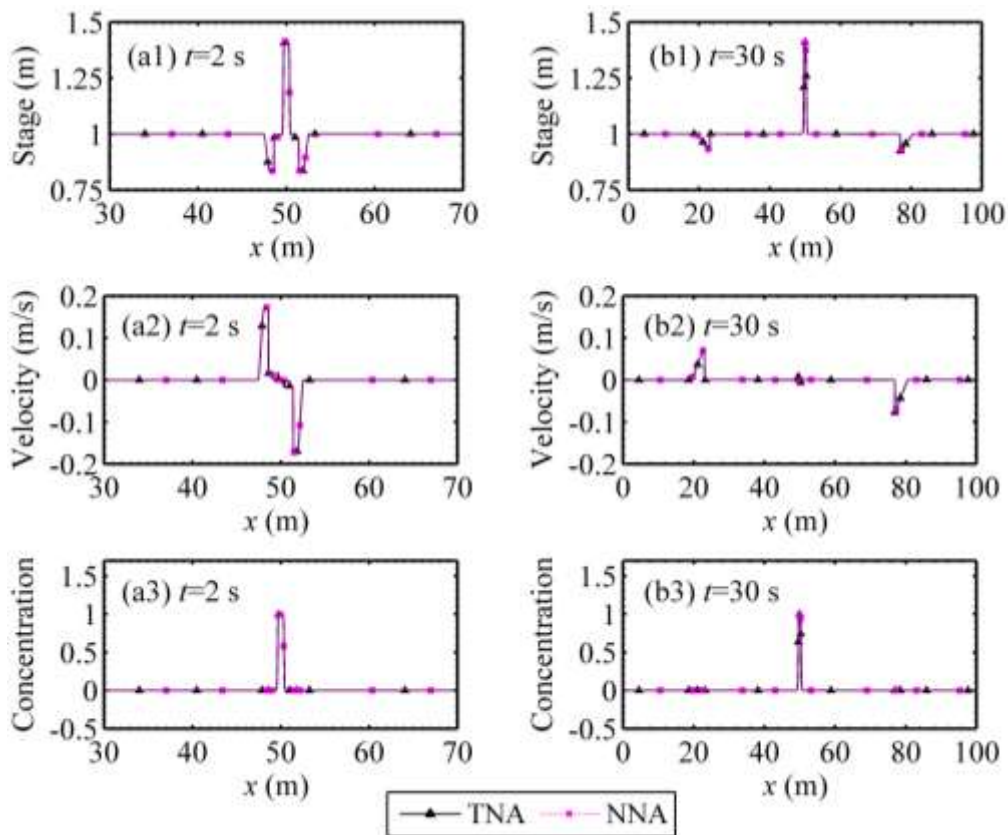
344 *3.3 Cases 3a and 3b: Density dam break with two initial discontinuities*

345 Case 3 considers a density dam break in a channel with fixed horizontal bed, containing a central
346 region of different density to that elsewhere in the channel. The channel is 100 m long and the
347 region of different density is 1 m wide separated by two infinitesimally thin dams located at $x =$
348 249.5 and $x = 250.5$ m. Initially, the stage throughout the channel is 1 m, and the liquid densities
349 in the central region bounded by the dam walls are $\rho_{in} = 0.5$ (Case 3a) and 2 kg/m^3 (Case 3b)
350 with the initial interior concentration set to $c_{in} = 1$. Elsewhere the initial liquid density is set
351 to $\rho_{out} = 1 \text{ kg/m}^3$ with initial concentration $c_{out} = 0$.

352 Figures 6 and 7 show the stage, velocity, and concentration profiles for $\rho_{in} = 0.5$ and 2 kg/m^3
353 respectively, computed by FCNA and CNA. Figures 8 and 9 show the corresponding temporal
354 variations in stage, velocity and concentration at $x = 25, 50$ and 75 m (i.e. upstream of the first
355 dam, at the mid-point between the dams, and downstream of the second dam). The predicted
356 interactions between the denser liquid and less dense liquid by FCNA and CNA are almost
357 identical: the denser liquid moves inwards towards the centre of the channel, squeezing the less
358 dense region upwards for $\rho_{in} = 0.5 \text{ kg/m}^3$, whilst for $\rho_{in} = 2 \text{ kg/m}^3$, the denser liquid falls under
359 gravity, driving left and right shock-type bores into the adjacent less dense liquid. Computed
360 profiles of the temporal variations at selected sections for $\rho_{in} = 0.5$ and 2 kg/m^3 show opposite

361 behaviour in water surface and velocity (Figs. 8 and 9) because the relative density ρ_{in} / ρ_{out} is
 362 less and greater than 1.0 respectively. Tables IV and V list the values obtained for L_{hz} , L_u and L_c
 363 for Cases 3a and 3b. L_{hz} has values close to zero, indicating negligible discrepancies between the
 364 two algorithms at the selected sections and instants. The L_u and L_c values are within 4%, a
 365 limited discrepancy. Case 2 and Case 3 confirm that both FCNA and CNA provide acceptable
 366 solutions to the problems of dam break arising from discontinuous density gradients.

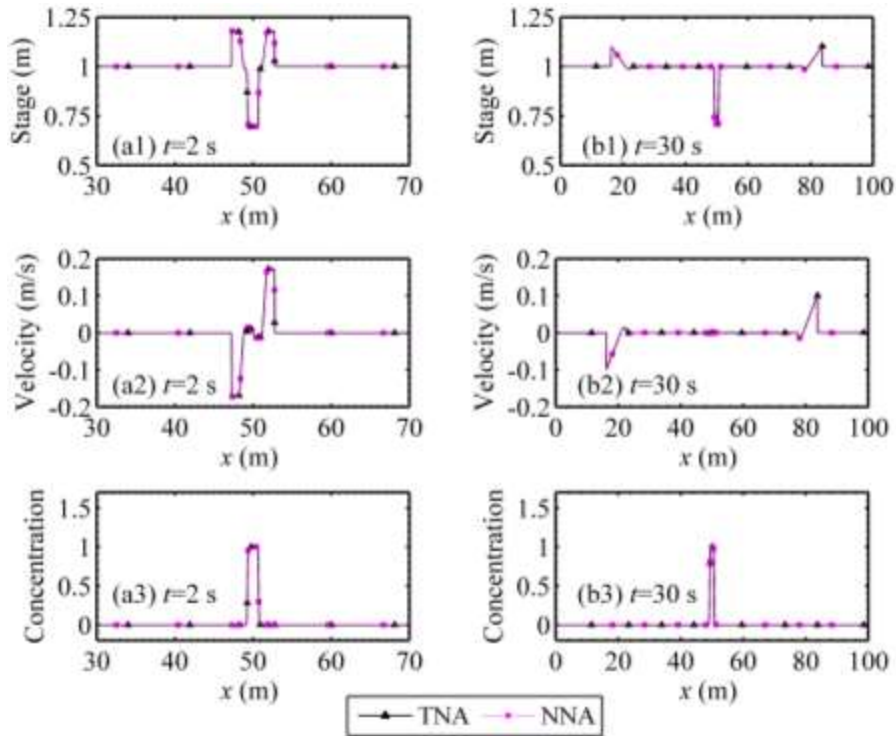
367



368

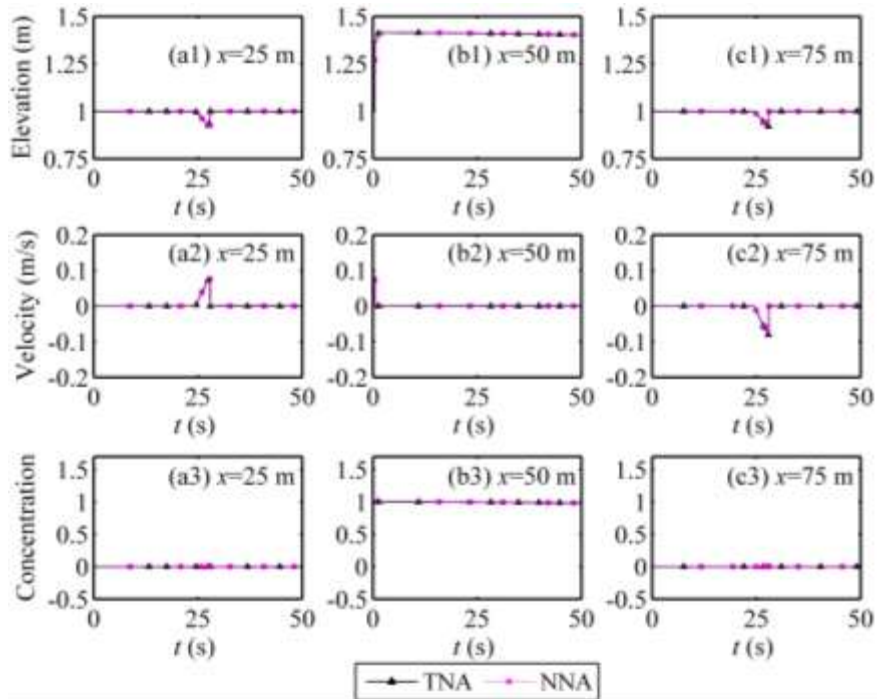
369 **Figure 6.** Case 3a: stage, velocity, and concentration profiles at times (a) $t = 2$ s and (b) $t = 30$ s,

370 predicted by FCNA and CNA for density dam break ($\rho_{in} = 0.5 \text{ kg/m}^3$) with two discontinuities.



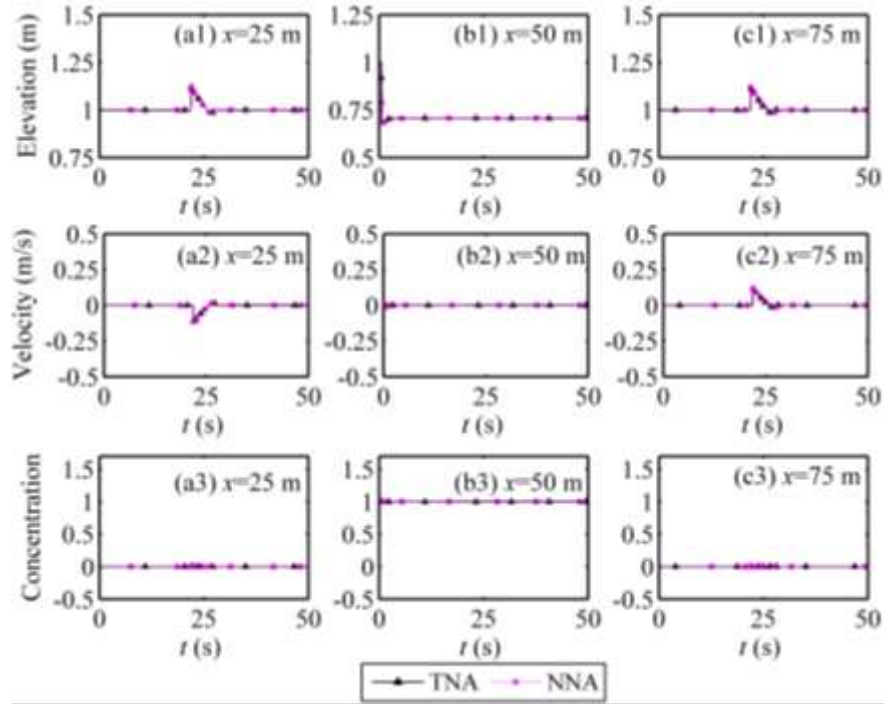
371
372
373
374

Figure 7. Case 3b: stage, velocity, and concentration profiles at times (a) $t = 2$ s and (b) $t = 30$ s, predicted by FCNA and CNA for density dam break ($\rho_m = 2.0 \text{ kg/m}^3$) with two discontinuities.



375
376
377
378

Figure 8. Case 3a: stage, velocity, and concentration time histories at locations (a) $x = 225$ m, and (b) $x = 275$ m, predicted by FCNA and CNA for density dam break ($\rho_m = 0.5 \text{ kg/m}^3$) with two discontinuities.



379
 380 **Figure 9.** Case 3b: Stage, velocity, and concentration time histories at locations (a) $x = 225$ m,
 381 and (b) $x = 275$ m, predicted by FCNA and CNA for density dam break ($\rho_{in} = 2.0 \text{ kg/m}^3$) with two
 382 discontinuities.

383
 384 **Table IV.** L_{hz} , L_u and L_c for Case 3a ($\rho_{in} = 0.5 \text{ kg/m}^3$)

Location or Time	$x = 25$ m	$x = 50$ m	$x = 75$ m	$t = 2$ s	$t = 30$ s
L_{hz} (%)	0.01	0.02	0.03	0.01	0.01
L_u (%)	0.69	N/A	0.56	3.79	2.19
L_c (%)	N/A	0.00	N/A	0.03	0.04

385
 386 **Table V.** L_{hz} , L_u and L_c for Case 3b ($\rho_{in} = 2.0 \text{ kg/m}^3$)

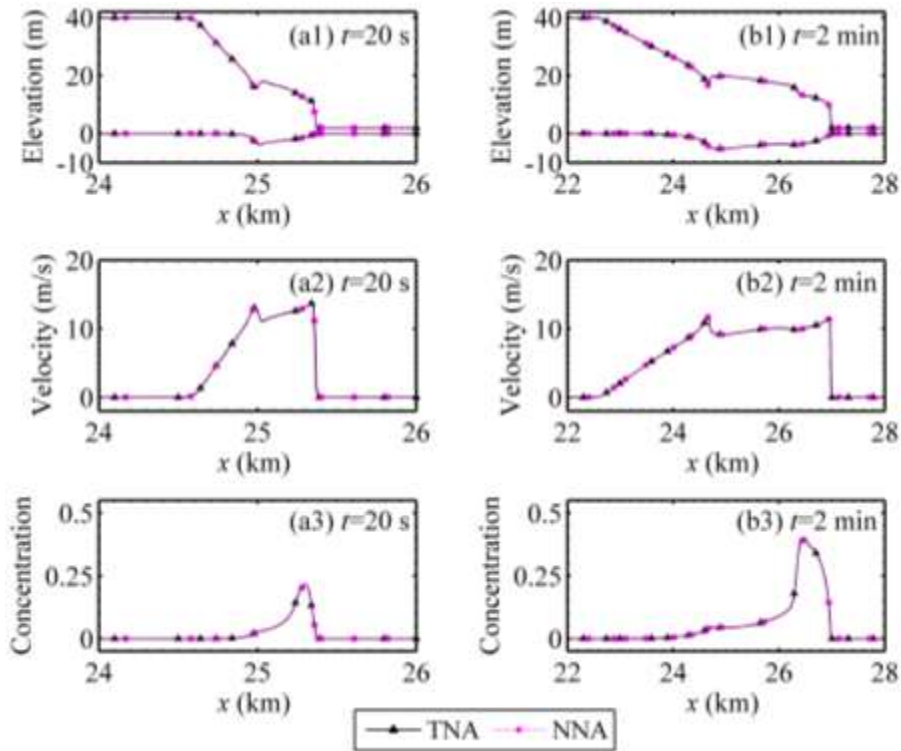
Location or Time	$x = 25$ m	$x = 50$ m	$x = 75$ m	$t = 2$ s	$t = 30$ s
L_{hz} (%)	0.02	0.03	0.02	0.01	0.03
L_u (%)	3.2	N/A	0.07	3.00	3.87
L_c (%)	N/A	0.00	N/A	0.27	0.02

387

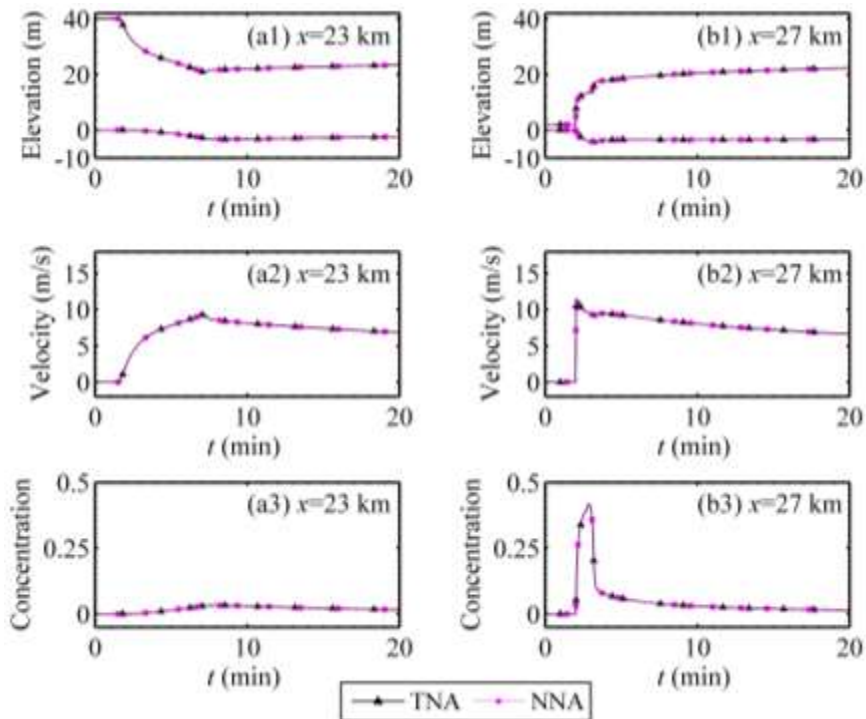
388 *3.4 Case 4: Dam-break over erodible beds of prototype scale*

389 Case 4 is used to test the relative performance of FCNA and CNA in modelling the mobile bed
390 hydraulics due to the instantaneous, full collapse of a dam. This test case was first proposed by
391 Cao et al. (2004) for a dam break in a long channel at prototype scale, with the simulation being
392 of relatively long duration. The dam is located at the centre of a 50-km-long channel. Initially, the
393 bed is horizontal and the static water depths upstream and downstream of the dam are 40 m and 2
394 m respectively. The duration of the numerical simulations was such that they were concluded
395 before forward and backward waves reached the downstream and upstream boundaries, so that the
396 boundary conditions could be simply set according to the initial static states. The same empirical
397 relationships are implemented for net sediment exchange flux as used by Cao et al. (2004).

398 Figure 10 compares longitudinal profiles of water surface, bed elevation, velocity and
399 concentration predicted by FCNA and CNA at two times after the initial dam break event. Figure
400 11 illustrates the temporal variations of stage, bed elevation, velocity, and concentration at
401 sections $x = 23$ and $x = 27$ km (i.e. 2 km upstream and downstream of the dam, respectively). It
402 can be seen that FCNA and CNA both give very similar predictions of the dam break process as it
403 evolves. Not only the location of the hydraulic jump ((a1) and (b1) in Fig. 10), but also the abrupt
404 fall in the free surface due to the existence of the contact discontinuity of sediment concentration
405 ((a3) and (b3) in Fig. 10) are properly modelled by the FCNA. It should be noted that the sharp
406 concentration gradient at the wavefront ((a3) and (b3) in Fig. 10) is modelled by the second term
407 of the second component of Eq. (6d) by the CNA, whereas it is incorporated in the mixture
408 density variation term ρh by the FCNA. Table VI lists values of L_{hz} , L_z , L_u and L_c , which are
409 within 0.5%, 1%, 1% and 1.5% respectively at the selected sections and instants, demonstrating
410 that the discrepancies between the FCNA and CNA are hardly distinguishable.



411
 412 **Figure 10.** Case 4: dam break over an erodible bed at prototype scale: profiles of (a) water surface
 413 and bed elevation, (b) velocity, and (c) concentration predicted by FCNA and CNA at times $t = 20$
 414 s and 2 min.



415
 416 **Figure 11.** Case 4: dam break over an erodible bed at prototype scale: time histories of (a) water
 417 surface and bed elevation, (b) velocity, and (c) concentration predicted by FCNA and CNA at
 418 locations $x = 23$ km and 27 km.

419

420 **Table VI.** L_{hz} , L_z , L_u and L_c for Case 4

Location or Time	$x = 23$ km	$x = 27$ km	$t = 20$ s	$t = 2$ min
L_{hz} (%)	0.30	0.30	0.00	0.01
L_z (%)	0.30	0.54	0.76	0.43
L_u (%)	0.07	0.12	0.55	0.25
L_c (%)	0.25	0.48	1.47	0.73

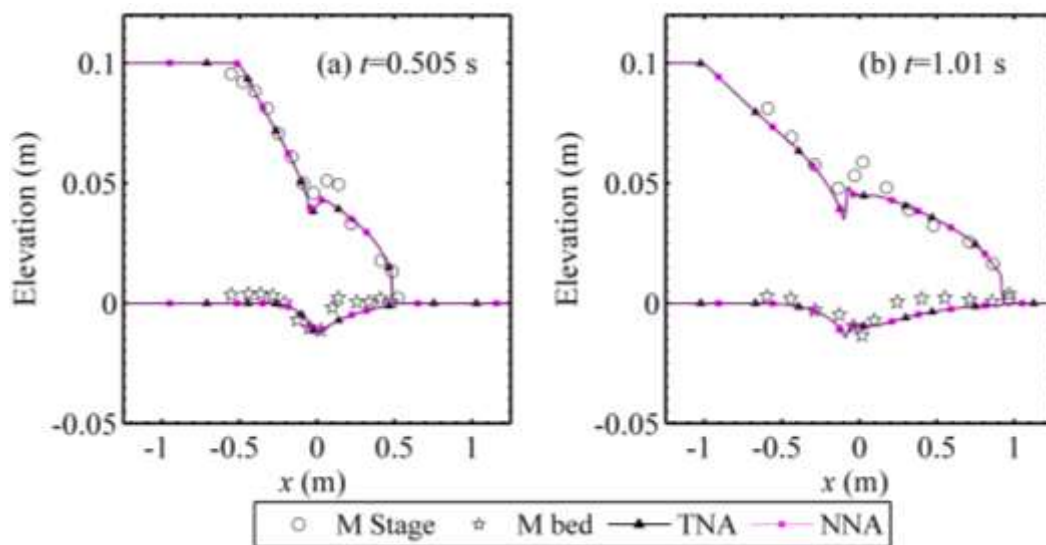
421

422 *3.5 Case 5: Experimental dam-break over erodible beds*

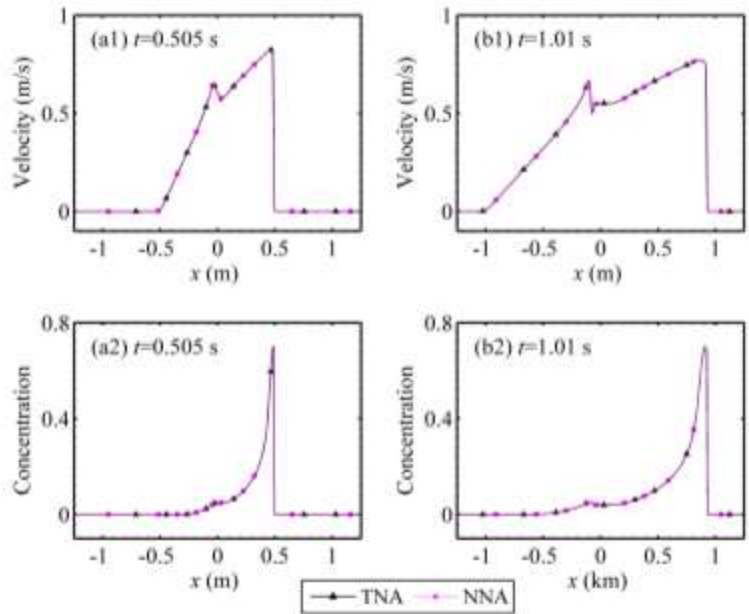
423 Laboratory experiments of dam break flow over a mobile bed reported in the literature include
 424 those of Capart and Young 1998, Fraccarollo and Capart 2002, Spinewine and Zech 2007, and
 425 Zech et al. 2008. Case 5, considered here, is that of Fraccarollo and Capart (2002) who conducted
 426 dam break tests in a channel 2.5 m long, 0.1 m wide and 0.25 m deep. The initial static water
 427 depths upstream and downstream of the dam were 0.1 m and 0 m respectively. In the numerical
 428 models, the boundary conditions are set to be the same as for Case 4. The net sediment exchange
 429 flux is determined following Cao et al. (2011b) with **modification coefficients** $\beta = 9$ and $\varphi = 3$.
 430 Tables I and II list the remaining model parameters.

431 Figure 12 shows measured and predicted stage and bed elevation profiles along a 2.5 m reach of
 432 the channel at times $t = 0.505$ and 1.01 s after the dam break. Figure 13 displays the
 433 corresponding velocity and concentration profiles. The agreement between the FCNA and CNA
 434 simulations and the experimental measurements is fairly good; **the initial bore and rarefaction**
 435 **waves match well, though there is some slight discrepancy between the measured and predicted**
 436 **reflected wave that seems trapped as a hydraulic jump at the location of the original dam break.**
 437 **This wave reflects from the bed as it is eroded, and its magnitude is underestimated by the FCNA**
 438 **and CNA numerical models (both of which give almost identical results).** The velocity and

439 concentration profiles are both characterized by an abrupt fall in velocity a sharp spike in
 440 concentration at the initial bore front as it propagates downstream. Figure 14 compares the FCNA
 441 and CNA predicted stage, bed elevation, velocity, and concentration time series at $x = -0.05$ and
 442 $x = 0.05$ m (0.05 m upstream and downstream of the initial dam respectively). The close
 443 agreement between the FCNA and CNA results is corroborated quantitatively in Table VII by the
 444 values of L_{hz} , L_z , L_u and L_c that are all within 1.5%. Meanwhile, the FCNA and CNA results
 445 both display similar differences to the measured stage (as mentioned above) leading to values of
 446 L_{hz}^* of 7.41% for FCNA and 7.38% for CNA at $t = 0.505$ s and 8.86% and 8.90% at $t = 1.01$ s,
 447 respectively. The results from Case 4 (involving large temporal and spatial scales) and Case 5
 448 (involving experimental data at laboratory scale) help provide confidence in the FCNA as a model
 449 for highly unsteady shallow flows with shock waves and sediment transport.

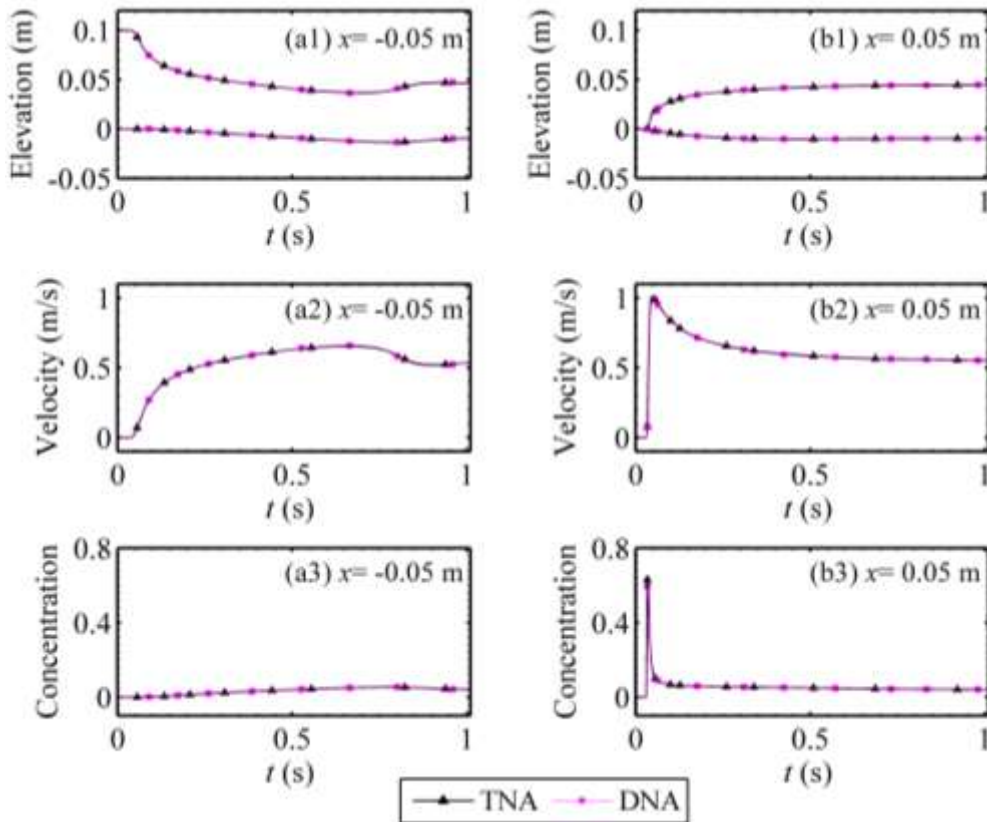


450
 451 **Figure 12.** Case 5: computed (FCNA and CNA) and measured (Fraccarollo and Capart, 2002)
 452 water surface and bed elevation profiles at (a) $t = 0.505$ and (b) $t = 1.01$ s for a dam break over an
 453 erodible bed.



454
455
456
457
458

Figure 13. Case 5: computed (FCNA and CNA) and measured (Fraccarollo and Capart, 2002) water surface and bed elevation profiles at (a) $t = 0.505$ and (b) $t = 1.01$ s for a dam break over an erodible bed.



459
460
461
462

Figure 14. Case 5: computed (FCNA and CNA) and measured (Fraccarollo and Capart, 2002) water surface, bed elevation, velocity, and concentration time series at (a) $x = -0.05$ m and (b) $x = 0.05$ m for a dam break over an erodible bed.

464 **Table VII.** L_{hz} , L_z , L_u , L_c and L_{hz}^* for Case 5

Location or Time	$x = -0.05$ m	$x = 0.05$ m	$t = 0.505$ s	$t = 1.01$ s
L_{hz} (%)	0.92	0.92	0.34	0.10
L_z (%)	0.94	0.86	0.57	0.59
L_u (%)	0.43	0.38	0.13	0.19
L_c (%)	0.70	1.38	0.58	0.51
L_{hz}^* of FCNA (%)	N/A	N/A	7.41	8.86
L_{hz}^* of CNA (%)	N/A	N/A	7.38	8.90

465

466 *3.6 Case 6: Flood flow due to landslide dam failure*

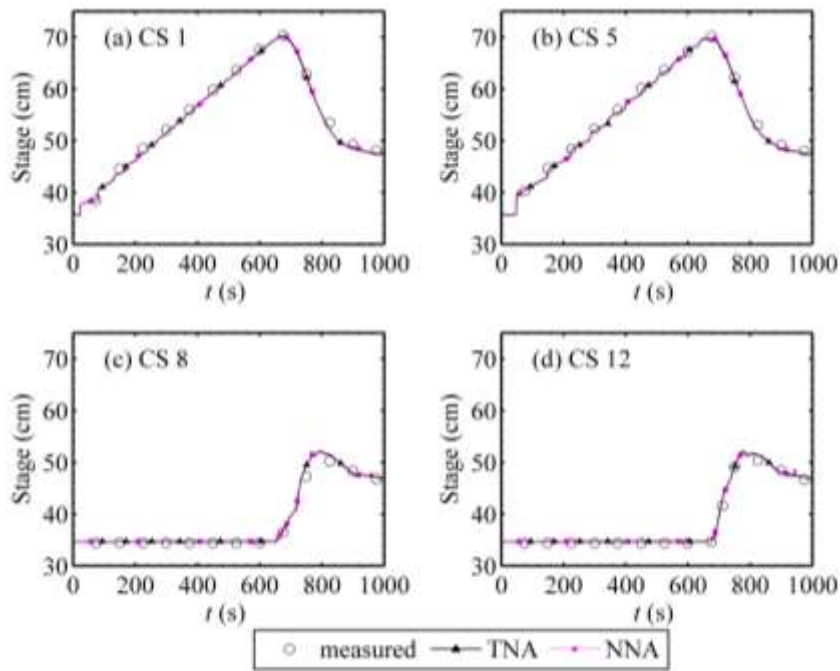
467 Landslide dam failures involve wet-dry fronts propagating over irregular bed topography, and so
468 constitute prime test cases by which to evaluate and compare the FCNA and CNA models in
469 terms of their well-balanced properties and their treatment of wet-dry interfaces, in addition to
470 shock capturing. Cao et al. (2011a) document results from a series of flume experiments on
471 landslide dam breaches and subsequent flood wave propagation in a large-scale flume of
472 dimensions $80 \text{ m} \times 1.2 \text{ m} \times 0.8 \text{ m}$ and a **fixed** bed slope of 0.001. The experiments were
473 implemented for different types of dams (i.e. with and without an initial breach) and dam material
474 compositions in order to provide a unique, systematic set of measured data for validating
475 numerical models of dam breaches and the resulting floods.

476 To demonstrate the performance of the FCNA, a uniform sediment case with no initial breach, i.e.,
477 F-case 15 (Cao et al. 2011a), is revisited here as Case 6. In this case, the dam was located at 41 m
478 from the flume inlet, was 0.4 m high and had a crest width of 0.2 m. The initial upstream and
479 downstream slopes of the dam were 1:4 and 1:5, respectively. The initial static water depths

480 immediately upstream and downstream of the dam were 0.054 m and 0.048 m respectively. The
481 inlet flow discharge was $0.025 \text{ m}^3/\text{s}^{-1}$, and no sediment was present. A 0.15 m high weir was
482 situated at the outlet of the laboratory flume, and so a transmissive condition was imposed at the
483 downstream boundary of the numerical models. Following Cao et al. (2011b), the net sediment
484 exchange flux is determined with modification coefficients $\beta = 9$ and $\varphi = 3$ for both FCNA and
485 CNA.

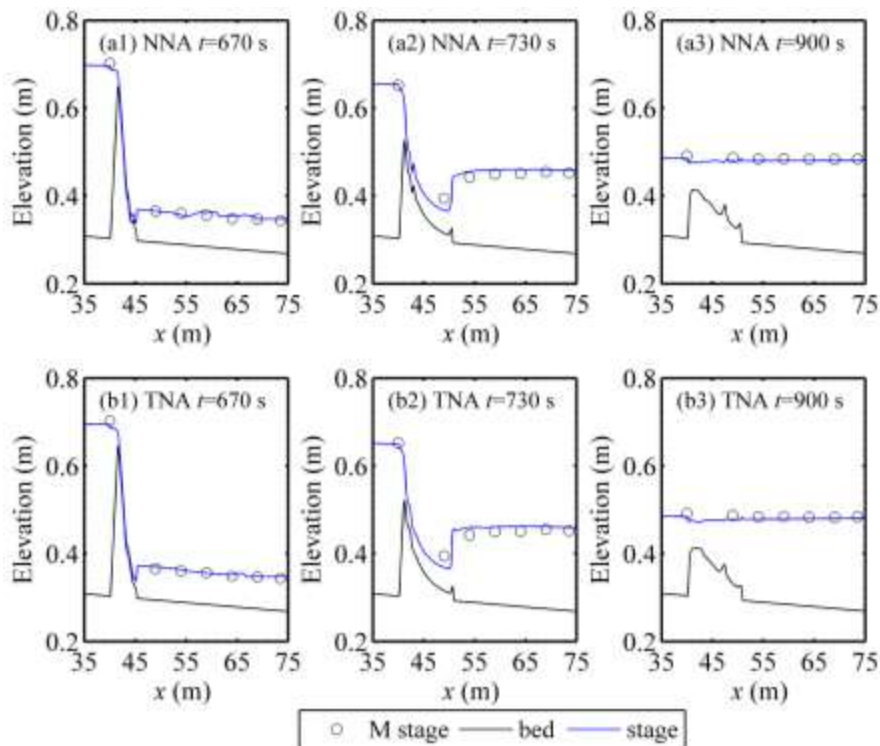
486 Figure 15 shows the predicted and measured stage hydrographs at selected cross sections. For F-
487 case 15, cross-sections CS1 and CS5 are 22 m and 1 m upstream of the dam, whilst cross-sections
488 CS8 and CS12 are 13 m and 32.5 m downstream of the dam. The stage hydrographs computed by
489 FCNA and CNA are both in good agreement with the measured data from Cao et al. (2011a).
490 Figure 16 presents the predicted water surface and bed profiles along with the measured stage at
491 times $t = 670, 730$ (shortly after the erosion of the dam) and 900 s (nearly final state of the dam
492 failure). It is hard to say which algorithm better reproduces the processes of the dam failure as
493 both the simulations of NNA and TNA match the measured data very well and the differences
494 between the results of the two algorithms are too subtle to distinguish. Echoing Figs. 15 and 16,
495 the values of the L_{hz}^* in Table VIII provide further insight into the relative performances of FCNA
496 and CNA in comparison with the measured stage. The values of L_{hz}^* are around 1% at the selected
497 sections but increase to around 8% at selected instants, which may be ascribed to the density of
498 scattered measured data. However, the values of L_{hz}^* in Table VIII also demonstrate the stage is
499 predicted by FCNA and CNA to almost the same accuracy, which further confirms that both
500 algorithms can successfully deal with the complex flow and sediment transport processes
501 associated with contact discontinuities as they propagate over irregular topographies.

502



503
504
505
506

Figure 15. Case 6: predicted (FCNA and CNA) and measured (Cao et al. 2011a) stage hydrographs at four cross-sections for a channel flow induced by a landslide dam failure at laboratory-scale.



507
508
509
510

Figure 16. Case 6: predicted (FCNA and CNA) water surface and bed profiles, and measured stage profiles (Cao et al. 2011a), at times $t = 670, 770$ and 870 s for channel flow induced by a landslide dam failure at laboratory-scale.

511

512 **Table VIII.** L_{hz}^* for Case 6

Location or Time	CS 1	CS 5	CS 8	CS 12	$t = 670$ s	$t = 730$ s	$t = 900$ s
L_{hz}^* of FCNA (%)	0.90	0.81	1.12	1.05	7.00	8.53	9.82
L_{hz}^* of CNA (%)	1.09	0.97	1.09	0.99	7.57	8.98	10.10

513

514

515 **4. Conclusion**

516 A numerical algorithm, FCNA, has been presented to solve the coupled SHSM equations directly,
517 based on an unmodified full conservation form of the equations with mixture density maintained
518 on the LHS of the equation set. When implemented with the well-balanced WSDGM version of
519 the SLIC scheme, FCNA performed satisfactorily for the following series of test cases: steady
520 equilibrium flow over a steep hump, density dam breaks with single and multiple discontinuities,
521 dam breaks over erodible beds at prototype and laboratory scale, and a flood flow due to a
522 landslide dam failure. It was demonstrated that the FCNA algorithm properly modelled
523 complicated flows with sharp fronts (in stage and velocity), sediment transport processes with
524 contact discontinuities over irregular topographies, and non-equilibrium bed morphological
525 change. Moreover, it was found that the conventional CNA, based on redistribution of the water-
526 sediment mixture density term, achieved very similar accuracy to the FCNA over the range of
527 verification and validation tests considered. These findings indicate that both the FCNA and
528 CNA algorithms can be satisfactorily applied in computational river modelling.

529

530

531 **Acknowledgements**

532 The work reported in this manuscript is funded by Natural Science Foundation of China
533 (Grants No. 51279144 and 11432015).

534

535

536 **References**

537 Aureli, F., Maranzoni, A. and Mignosa, P. (2004), "Two dimensional modeling of rapidly varying
538 flows by finite volume schemes", *River Flow*, pp. 837-847.

539 Aureli, F., Maranzoni, A., Mignosa, P. and Ziveri, C. (2008), "A weighted surface-depth gradient
540 method for the numerical integration of the 2D shallow water equations with topography",
541 *Advances in Water Resources*, Vol. 31 No. 7, pp. 962-974.

542 Batchelor, G K. (1967), *An Introduction to Fluid Dynamics*, Cambridge University Press, England.

543 Bellos, C. V., Soulis, V. and Sakkas, J. G (1992), "Experimental investigation of two-dimensional
544 dam-break induced flows", *Journal of Hydraulic Research*, Vol. 30 No. 1, pp. 47-63.

545 Bermudez, A. and Vazquez, M. E. (1994), "Upwind methods for hyperbolic conservation laws with
546 source terms", *Computers & Fluids*, Vol. 23 No. 8, pp. 1049-1071.

547 Cao, Z., Li, J., Pender, G and Liu, Q. (2015), "Whole-Process Modeling of Reservoir Turbidity
548 Currents by a Double layer-Averaged Model", *Journal of Hydraulic Engineering*, Vol. 141 No.
549 2, pp. 04014069.

550 Cao, Z., Pender, G, Wallis, S. and Carling, P. (2004), "Computational dam-break hydraulics over
551 erodible sediment bed", *Journal of Hydraulic Engineering*, Vol. 130 No. 7, pp. 689-703.

552 Cao, Z., Yue, Z. and Pender, G (2011a), "Landslide dam failure and flood hydraulics. Part I:
553 experimental investigation", *Natural Hazards*, Vol. 59 No. 2, pp. 1003-1019.

554 Cao, Z., Yue, Z. and Pender, G (2011b), "Landslide dam failure and flood hydraulics. Part II: coupled
555 mathematical modelling", *Natural Hazards*, Vol. 59 No. 2, pp. 1021-1045.

556 Capart, H. and Young, D. L. (1998), "Formation of a jump by the dam-break wave over a granular
557 bed", *Journal of Fluid Mechanics*, Vol. 372 No. 165-187.

558 Cea, L. and Vázquez-Cendón, M. E. (2010), "Unstructured finite volume discretization of two-
559 dimensional depth-averaged shallow water equations with porosity", *International Journal for*
560 *Numerical Methods in Fluids*, Vol. 63 No. 8, pp. 903-930.

561 Fraccarollo, L. and Capart, H. (2002), "Riemann wave description of erosional dam-break flows",

- 562 *Journal of Fluid Mechanics*, Vol. 461, pp. 183-228.
- 563 Fraccarollo, L. and Toro, E. F. (1995), "Experimental and numerical assessment of the shallow water
564 model for two-dimensional dam-break type problems", *Journal of Hydraulic Research*, Vol. 33
565 No. 6, pp. 843-864.
- 566 Gear, C. W. (1971), *Numerical Initial Value Problems in Ordinary Differential Equations*, Prentice
567 Hall PTR Upper Saddle River, New Jersey, USA.
- 568 Gottlieb, S. and Shu, C. W. (1998), "Total variation diminishing Runge-Kutta schemes", *Mathematics
569 of computation*, Vol. 67 No. 221, pp. 73-85.
- 570 Harten, A., Lax, P. D. and van Leer, B. (1983), "On upstream differencing and Godunov-type schemes
571 for hyperbolic conservation laws", *SIAM Review*, Vol. 25 No. 1, pp. 35-61.
- 572 Hu, P. and Cao, Z. (2009), "Fully coupled mathematical modeling of turbidity currents over erodible
573 bed", *Advances in Water Resources*, Vol. 32 No. 1, pp. 1-15.
- 574 Hu, P., Cao, Z., Pender, G and Tan, G (2012), "Numerical modelling of turbidity currents in the
575 Xiaolangdi reservoir, Yellow River, China", *Journal of Hydrology*, Vol. 464-465 No. 0, pp. 41-
576 53.
- 577 Hu, P., Li, W., He, Z., Päht, T. and Yue, Z. (2015), "Well-balanced and flexible morphological
578 modeling of swash hydrodynamics and sediment transport", *Coastal Engineering*, Vol. 96, pp.
579 27-37.
- 580 Huang, W., Cao, Z., Carling, P. and Pender, G (2014), "Coupled 2D Hydrodynamic and Sediment
581 Transport Modeling of Megaflood due to Glacier Dam-break in Altai Mountains, Southern
582 Siberia", *Journal of Mountain Science*, Vol. 11 No. 6, pp. 1442-1453.
- 583 Huang, W., Cao, Z., Yue, Z., Pender, G and Zhou, J. (2012), "Coupled modelling of flood due to
584 natural landslide dam breach", *Proceedings of the ICE - Water Management*, Vol. 165 No. 10,
585 pp. 525-542.
- 586 Kim, D.-H. (2015), "H2D morphodynamic model considering wave, current and sediment interaction",
587 *Coastal Engineering*, Vol. 95, pp. 20-34.
- 588 Kim, J., Ivanov, V. Y. and Katopodes, N. D. (2013), "Modeling erosion and sedimentation coupled
589 with hydrological and overland flow processes at the watershed scale", *Water Resources
590 Research*, Vol. 49 No. 9, pp. 5134-5154.
- 591 Leal, J. G A. B., Ferreira, R. M. L. and Cardoso, A. H. (2006), "Dam-Break Wave-Front Celerity ",
592 *Journal of Hydraulic Engineering*, Vol. 132 No. 1, pp. 69-76.
- 593 Leighton, F. Z., Borthwick, A. G L. and Taylor, P. H. (2010), "1-D numerical modelling of shallow

594 flows with variable horizontal density", *International Journal for Numerical Methods in Fluids*,
595 Vol. 62 No. 11, pp. 1209-1231.

596 Li, S. and Duffy, C. J. (2011), "Fully coupled approach to modeling shallow water flow, sediment
597 transport, and bed evolution in rivers", *Water Resources Research*, Vol. 47 No. 3, pp. 1-20.

598 Li, W., van Maren, D. S., Wang, Z. B., de Vriend, H. J. and Wu, B. (2014), "Peak discharge increase in
599 hyperconcentrated floods", *Advances in Water Resources*, Vol. 67, pp. 65-77.

600 Liang, Q. and Borthwick, A. (2009), "Adaptive quadtree simulation of shallow flows with wet-dry
601 fronts over complex topography", *Computers and Fluids*, Vol. 38 No. 2, pp. 221-234.

602 Liang, Q. and Marche, F. (2009), "Numerical resolution of well-balanced shallow water equations with
603 complex source terms", *Advances in Water Resources*, Vol. 32 No. 6, pp. 873-884.

604 Liska, R. and Wendroff, B. (1998), "Composite Schemes for Conservation Laws", *SIAM J. Numer.
605 Anal.*, Vol. 35 No. 6, pp. 2250-2271.

606 Qian, H., Cao, Z., Pender, G., Liu, H. and Hu, P. (2015), "Well-balanced numerical modelling of non-
607 uniform sediment transport in alluvial rivers", *International Journal of Sediment Research*, Vol.
608 30 No. 2, pp. 117-130.

609 Roe, P. L. (1981), "Approximate Riemann Solvers, Parameter Vectors and Difference Schemes",
610 *Journal of computational physics*, Vol. 43 No. 2, pp. 357-372.

611 Rogers, B. D., Borthwick, A. G L. and Taylor, P. H. (2003), "Mathematical balancing of flux gradient
612 and source terms prior to using Roe's approximate Riemann solver", *Journal of Computational
613 Physics*, Vol. 192 No. 2, pp. 422-451.

614 Simpson, G and Castellort, S. (2006), "Coupled model of surface water flow, sediment transport and
615 morphological evolution", *Computers & Geosciences*, Vol. 32 No. 10, pp. 1600-1614.

616 Spinewine, B. and Zech, Y. (2007), "Small-scale laboratory dam-break waves on movable beds",
617 *Journal of Hydraulic Research*, Vol. 45 No. sup1, pp. 73-86.

618 Toro, E. F. (1999), *Riemann solvers and numerical methods for fluid dynamics*, Springer-Verlag,
619 Germany.

620 Toro, E. F. (2001), *Shock-capturing methods for free-surface shallow flows*, John Wiley, England.

621 Toro, E. F., Spruce, M. and Speares, W. (1994), "Restoration of the contact surface in the HLL-
622 Riemann solver", *Shock waves* Vol. 4, pp. 25-34.

623 Wu, W. (2007), *Computational river dynamics*, Taylor & Francis, London.

624 Wu, W., Marsooli, R. and He, Z. (2012), "Depth-averaged two-dimensional model of unsteady flow
625 and sediment transport due to noncohesive embankment break/breaching", *Journal of Hydraulic*

- 626 *Engineering*, Vol. 138 No. 6, pp. 503-516.
- 627 Wu, W. and Wang, S. (2008), "One-dimensional explicit finite-volume model for sediment transport",
628 *Journal of Hydraulic Research*, Vol. 46 No. 1, pp. 87-98.
- 629 Wu, W. and Wang, S. S. Y. (2007), "One-dimensional modeling of dam-break flow over movable
630 beds", *Journal of Hydraulic Engineering*, Vol. 133 No. 1, pp. 48-58.
- 631 Xia, J., Lin, B., Falconer, R. A. and Wang, G (2010), "Modelling dam-break flows over mobile beds
632 using a 2D coupled approach", *Advances in Water Resources*, Vol. 33 No. 2, pp. 171-183.
- 633 Xiao, H., Young, Y. and Prévost, J. H. (2010), "Hydro- and morpho-dynamic modeling of breaking
634 solitary waves over a fine sand beach. Part II: Numerical simulation", *Marine Geology*, Vol. 269
635 No. 3-4, pp. 107-118.
- 636 Xie, J. ed. (1990), *River Modelling*. China Water and Power Press, Beijing (in Chinese).
- 637 Yue, Z., Liu, H., Li, Y., Hu, P. and Zhang, Y. (2015), "A Well-Balanced and Fully Coupled
638 Noncapacity Model for Dam-Break Flooding", *Mathematical Problems in Engineering*, Vol.
639 2015, pp. 1-13.
- 640 Yue, Z., Cao, Z., Li, X. and Che, T. (2008), "Two-dimensional coupled mathematical modeling of
641 fluvial processes with intense sediment transport and rapid bed evolution", *Science in China*
642 *Series G: Physics Mechanics and Astronomy*, Vol. 51 No. 9, pp. 1427-1438.
- 643 Zech, Y., Soares-Frazao, S., Spinewine, B. and Grelle, N. L. (2008), "Dam-break induced sediment
644 movement: Experimental approaches and numerical modelling", *Journal of Hydraulic*
645 *Research*, Vol. 46 No. 2, pp. 176-190.
- 646 Zhang, S. and Duan, J. G (2011), "1D finite volume model of unsteady flow over mobile bed",
647 *Journal of Hydrology*, Vol. 405 No. 1-2, pp. 57-68.
- 648 Zhou, J. G, Causon, D. M., Mingham, C. G and Ingram, D. M. (2001), "The surface gradient method
649 for the treatment of source terms in the shallow-water equations", *Journal of Computational*
650 *Physics*, Vol. 168 No. 1, pp. 1-25.
- 651 Zhu, F. and Dodd, N. (2015), "The morphodynamics of a swash event on an erodible beach", *Journal*
652 *of Fluid Mechanics*, Vol. 762, pp. 110-140.
- 653
- 654
- 655 **Corresponding author**
- 656 Professor Zhixian Cao can be contacted at: zxcao@whu.edu.cn

657 **List of Tables**

658 **Table I.** Spatial increment and Courant number used in test cases

Test case	1	2	3	4	5	6
Spatial step Δx (m)	0.05	0.02	0.02	10	0.005	0.04
Courant number C_r	0.95	0.95	0.95	0.95	0.95	0.95

659

660 **Table II.** Summary of test cases

Test case	Sediment density ρ_s (kg/m ³)	Water density ρ_w (kg/m ³)	Gravitational acceleration g (m/s ²)	Sediment diameter d (mm)	Manning roughness n	Sediment porosity p
1	2,650	1,000	9.8	N/A	0.0	N/A
2	10.0	1.0	1.0	N/A	0.0	N/A
3	0.5&2.0	1.0	1.0	N/A	0.0	N/A
4	2,650	1,000	9.8	8.0	0.03	0.4
5*	1,540	1,000	9.8	3.5	0.025	0.3
6*	2,650	1,000	9.8	0.8	0.012	0.4

661 Notes: * Cases using measured data.

662

663 **Table III.** L_{hz} , L_u and L_c for Case 2

Location or Time	$x = 225$ m	$x = 275$ m	$t = 30$ s	$t = 100$ s
L_{hz} (%)	0.01	2.24	0.30	0.68
L_u (%)	0.02	2.07	2.92	1.95
L_c (%)	0.00	1.93	0.17	0.33

664

665 **Table IV.** L_{hz} , L_u and L_c for Case 3a ($\rho_{in} = 0.5 \text{ kg/m}^3$)

Location or Time	$x = 25 \text{ m}$	$x = 50 \text{ m}$	$x = 75 \text{ m}$	$t = 2 \text{ s}$	$t = 30 \text{ s}$
L_{hz} (%)	0.01	0.02	0.03	0.01	0.01
L_u (%)	0.69	N/A	0.56	3.79	2.19
L_c (%)	N/A	0.00	N/A	0.03	0.04

666

667 **Table V.** L_{hz} , L_u and L_c of Case 3b ($\rho_{in} = 2.0 \text{ kg/m}^3$)

Location or Time	$x = 25 \text{ m}$	$x = 50 \text{ m}$	$x = 75 \text{ m}$	$t = 2 \text{ s}$	$t = 30 \text{ s}$
L_{hz} (%)	0.02	0.03	0.02	0.01	0.03
L_u (%)	3.2	N/A	0.07	3.00	3.87
L_c (%)	N/A	0.00	N/A	0.27	0.02

668

669 **Table VI.** L_{hz} , L_z , L_u and L_c for Case 4

Location or Time	$x = 23 \text{ km}$	$x = 27 \text{ km}$	$t = 20 \text{ s}$	$t = 2 \text{ min}$
L_{hz} (%)	0.30	0.30	0.00	0.01
L_z (%)	0.30	0.54	0.76	0.43
L_u (%)	0.07	0.12	0.55	0.25
L_c (%)	0.25	0.48	1.47	0.73

670

671 **Table VII.** L_{hz} , L_z , L_u , L_c and L_{hz}^* for Case 5

Location or Time	$x = -0.05$ m	$x = 0.05$ m	$t = 0.505$ s	$t = 1.01$ s
L_{hz} (%)	0.92	0.92	0.34	0.10
L_z (%)	0.94	0.86	0.57	0.59
L_u (%)	0.43	0.38	0.13	0.19
L_c (%)	0.70	1.38	0.58	0.51
L_{hz}^* of FCNA (%)	N/A	N/A	7.41	8.86
L_{hz}^* of CNA (%)	N/A	N/A	7.38	8.90

672

673 **Table VIII.** L_{hz}^* for Case 6

Location or Time	CS 1	CS 5	CS 8	CS 12	$t = 670$ s	$t = 730$ s	$t = 900$ s
L_{hz}^* of FCNA (%)	0.90	0.81	1.12	1.05	7.00	8.53	9.82
L_{hz}^* of CNA (%)	1.09	0.97	1.09	0.99	7.57	8.98	10.10

674

675 **List of figure captions**

676 **Figure 1.** Sketch of the WSDGM version of the SLIC scheme

677

678 **Figure 2.** Case 1a: equilibrium stage and velocity profiles predicted by FCNA and CNA for initial
679 stage of 1.0 m

680

681 **Figure 3.** Case 1b: equilibrium stage and velocity profiles predicted by FCNA and CNA for
682 initial stage of 0.5 m

683

684 **Figure 4.** Case 2: stage and velocity profiles predicted by FCNA and CNA for density dam break
685 with a single discontinuity at times: (a) $t = 30$ s; and (b) $t = 100$ s.

686

687 **Figure 5.** Case 2: stage and velocity time histories predicted by FCNA and CNA for density dam
688 break with a single discontinuity at locations: (a) $x = 225$ m; and (b) $x = 275$ m.

689

690 **Figure 6.** Case 3a: stage, velocity, and concentration profiles at times (a) $t = 2$ s and (b) $t = 30$ s,
691 predicted by FCNA and CNA for density dam break ($\rho_{in} = 0.5$ kg/m³) with two discontinuities.

692

693 **Figure 7.** Case 3b: stage, velocity, and concentration profiles at times (a) $t = 2$ s and (b) $t = 30$ s,
694 predicted by FCNA and CNA for density dam break ($\rho_{in} = 2.0$ kg/m³) with two discontinuities.

695

696 **Figure 8.** Case 3a: stage, velocity, and concentration time histories at locations (a) $x = 225$ m, and
697 (b) $x = 275$ m, predicted by FCNA and CNA for density dam break ($\rho_{in} = 0.5$ kg/m³) with two
698 discontinuities.

699

700 **Figure 9.** Case 3b: Stage, velocity, and concentration time histories at locations (a) $x = 225$ m,
701 and (b) $x = 275$ m, predicted by FCNA and CNA for density dam break ($\rho_{in} = 2.0$ kg/m³) with two
702 discontinuities.

703

704 **Figure 10.** Case 4: dam break over an erodible bed at prototype scale: profiles of (a) water surface
705 and bed elevation, (b) velocity, and (c) concentration predicted by FCNA and CNA at times $t = 20$
706 s and 2 min.

707

708 **Figure 11.** Case 4: dam break over an erodible bed at prototype scale: time histories of (a) water
709 surface and bed elevation, (b) velocity, and (c) concentration predicted by FCNA and CNA at
710 locations $x = 23$ km and 27 km.

711

712 **Figure 12.** Case 5: computed (FCNA and CNA) and measured (Fraccarollo and Capart, 2002)
713 water surface and bed elevation profiles at (a) $t = 0.505$ and (b) $t = 1.01$ s for a dam break over an
714 erodible bed.

715

716 **Figure 13.** Case 5: computed (FCNA and CNA) and measured (Fraccarollo and Capart, 2002)
717 water surface and bed elevation profiles at (a) $t = 0.505$ and (b) $t = 1.01$ s for a dam break over an
718 erodible bed.

719

720 **Figure 14.** Case 5: computed (FCNA and CNA) and measured (Fraccarollo and Capart, 2002)
721 water surface, bed elevation, velocity, and concentration time series at (a) $x = -0.05$ m and (b) $x =$
722 0.05 m for a dam break over an erodible bed.

723

724 **Figure 15.** Case 6: predicted (FCNA and CNA) and measured (Cao et al. 2011a) stage
725 hydrographs at four cross-sections for a channel flow induced by a landslide dam failure at
726 laboratory-scale.

727

728

729 **Figure 16.** Case 6: predicted (FCNA and CNA) water surface and bed profiles, and measured
730 stage profiles (Cao et al. 2011a), at times $t = 670, 770$ and 870 s for channel flow induced by a
731 landslide dam failure at laboratory-scale.